Supporting Online Material for

Induced Homomorphism: Kirchhoff's Law in Photonics

Shuai Sun[1], Mario Miscuglio[1], Xiaoxuan Ma[1], Zhizhen Ma[1], Chen Shen [1], Engin Kayraklioglu[1], Jeffery Anderson[1], Tarek El Ghazawi[1], Volker J. Sorger*

[1] Department of Electrical and Computer Engineering, The George Washington University, Washington, DC 20052, USA

* Corresponding author sorger@gwu.edu

This PDF file includes:

1. **Inverse design of a KPN**
2. **Optical Finite Difference Method Mapping**
3. **Partial Differential Equation Classification**
4. **5×5 Finite Difference Method Simulation Models and Measurement Data**
5. **SPACE Runtime Analysis**
6. **Boundary Weighted SPACE Analysis**
7. **SPACE configuration library for solving heat transfer problem for different materials**
8. **Up-scaling Scaling Analysis**

Inverse design of a KPN

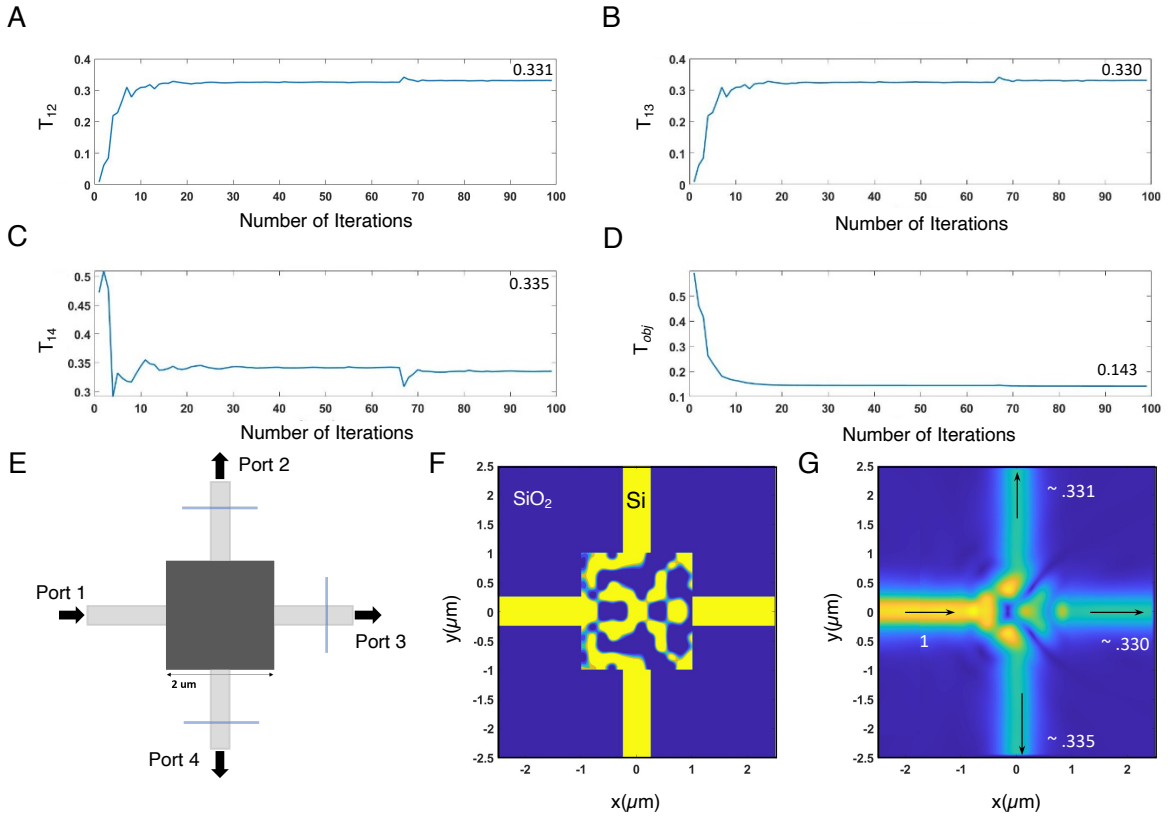

Figure S1. Iterative optimization process for obtaining inverse design of a 1:3 equal splitter. The optimization is based on the software package, Spins, (license through Stanford OTL) that uses an optimization algorithm to design arbitrary photonic devices according to the specified constrains. (**A-C**) Evolution of the transmittance during the optimization process. Here we show the transmittance for port 2 (T_{12}), port 3 (T_{13}) and port 4 (T_{14}). (**D**) Optimization of the cost function T_{Obj} as function of the number of iterations. (**E**) Initial design at iteration 0. The optimized structure lies in a footprint of 2x2 µm. (**F**) Optimized design of a 1:3 equal splitter. Coded in the colors the different refractive index. In blue SiO_2 (n_{SiO2} =1.444) and yellow Si (n_{Si}= 3.476) waveguide. (**G**) Normalized electric field distribution. The optical power of a TE mode propagating from port 1 is equally split in all the other ports (2-4). Reported at each port the percentage of the optical power delivered.

An optimized inverse design approach is used by setting the design area to 5 µm and the even splitting functionality in the cardinal directions according to the following cost function to optimize

$$\min T_{\text{obj}} = |T - Pout_2| + |T - Pout_3|^2 + |T - Pout_4|^2, \quad (1)$$

where T is the target transmittance and $Pout_n$ is the power at the port *n,* assuming the following constraints:

$$0 \leq Pout_2 + Pout_3 + Pout_4 \leq 1\ (Pout_1) \quad (2)$$

In the full space of fabricable devices, the optimization algorithm finds a structure (**Figure 2A.ii** of the main manuscript) that meets these requirements. (Further details of the electromagnetic characterization of the inverse design KPN can be found in the SOM, **Fig. S2**).

The inversely designed KPN is one among the infinite number of configurations that would satisfy the optimization of the cost function, and even if characterized by a compact size (2x2 μm), it is significantly more intricate to fabricate with the same high yield as regular photonics due to its limited size. Additionally, this type of node would require a completely different configuration and related optimization process for mimicking different 'optical power' partitioning, while the heuristic solution can be straightforwardly reconfigured by actively tuning the coupling coefficients with the ring resonators. It is worth noticing that the inverse design of a KPN is not symmetric, therefore when the input comes from a different port the power splitting is uneven. Ignoring non-idealities from fabrication steps, the KPN S-parameter matrix is perfectly equal to its transpose ($\boldsymbol{S} = \boldsymbol{S}^T$) leading to a reciprocal behavior, since it is a passive and linear structure free from magnetic poles.

1. Optical Finite Difference Method Mapping

In order to derive the governing equation for the Optical Finite Difference Method (OFDM), we started again from the general Laplace's equation (Eqn. 1) in a two-dimensional domain with P represents each node and ∇ indicates the gradient operator.

$$\nabla^2 P = \frac{\partial^2 P}{\partial x^2} + \frac{\partial^2 P}{\partial y^2} = 0 \tag{1}$$

Similar to the numerical FDM approach, the Optical FDM also uses mathematical difference approximations with equi-long small steps on both x and y directions and therefore, Eqn. 1 can be written as a set of the following, where i and j represent the node at (i,j) position in the mesh grid while $i\pm1$ and $j\pm1$ are the nodes one step next to it.

$$\frac{\partial^2 P}{\partial x^2} \cong \frac{P_{i+1,j} - 2P_{i,j} + P_{i-1,j}}{\Delta x^2} \tag{2}$$

$$\frac{\partial^2 P}{\partial y^2} \cong \frac{P_{i+1,j} - 2P_{i,j} + P_{i-1,j}}{\Delta y^2} \tag{3}$$

And since we assume equi-long steps, $\Delta x = \Delta y = \Delta$ can be substitute into Eqn. 1 with Eqn. 2 and 3 and yield

$$\nabla^2 P_{i,j} \cong P_{i+1,i} + P_{i-1,j} + P_{i,j+1} + P_{i,j-1} - 4P_{i,j} = 0 \tag{4}$$

This reveals the same conclusion as the numerical FDM that one center node can be represented by its four adjacent nodes with the same step size on both x- and y-axis and the final solution accuracy is directly proportional to the step size (i.e. mesh resolution in this case). However, there is a major difference between the numerical model and the optical model that needs to be considered. For example, in an electrical resistor mesh grid, the data readout at each node is simply the electrical potential between that node and the boundary (i.e. the ground) which is a scalar without any direction. Contrarily, in the optical model, the light intensity at each node, which we considered as the solution of the model, not only has the power level but also takes four different directions as the light propagates as we have shown in the main paper. In addition, it is nearly impossible to deploy an insusceptible measurement or data readout mechanism in optics, meaning at least a portion of the light intensity will be consumed to read the solution. Therefore, we choose to use 50/50 Y-junctions to tap out 50% of the light outflow in all four directions of the node while still keeping the rest of the light in the circuit to continue the calculation. The benefit of using Y-junction splitters is, different from other waveguide-integrated photodetectors, only one direction of the light can be detected which effectively separate the readout signal from the computing signal. With superscripts N, S, W, E represent the coupler readout at each direction, the FDM in our design is derived as

$$\nabla^2 P_{i,j} \cong 2\left(P^N_{i+1,j} + P^S_{i+1,j} + P^W_{i+1,j} + P^E_{i+1,j} + P^N_{i-1,j} + P^S_{i-1,j} + P^W_{i-1,j} + P^E_{i-1,j} + P^N_{i,j+1} + P^S_{i,j+1} + P^W_{i,j+1} + P^E_{i,j+1} + P^N_{i,j-1} + P^S_{i,j-1} + P^W_{i,j-1} + P^E_{i,j-1}\right) - 2(4P^N_{i,j} + 4P^S_{i,j} + 4P^W_{i,j} + 4P^E_{i,j}) \quad (5)$$

And the factor of 2 shown in Eqn.5 could be canceled out since all the data collected will be eventually normalized to unity. It also indicates that the splitting ratio at the Y-junction could be set to any ratios, and increasing the computing light portion could further improve the size scalability of SPACE as long as the coupled light for readout is enough to meet the minimum sensitivity of the detector according to the reading bandwidth, i.e. Noise Equivalent Power (of the inferred camera, like in our case, or integrated photodetector) .

It is important to clarify that, even though we mapped the traditional FDM to the optical domain, our proposed SPACE does not follow the numerical approach of the FDM. Instead, a PDE is mapped to our SPACE circuit on the hardware level and uses light intensity to emulate this problem and get a solution.

2. Partial Differential Equation Classification

Partial Differential Equations (PDEs) nowadays, as one of the most commonly used modeling methods for describing multivariable functions and their partial derivatives, have a wide range of applications and, of course, a variety of transformations. In this section we identify the specific category of the PDE that SPACE can solve.

Firstly, based on the highest order *m* of all the terms in the equation, PDE can be classified into linear PDE and nonlinear PDE (**Fig. S1**). For nonlinear PDEs in general, there is no governing rules or strategies to solve and each individual type of nonlinear PDEs always been treated as a separate problem with its own method. Thus, we mainly focus on the linear PDEs in this paper in order to find a more generic way of solving them in the optical domain.

Secondly, within the linear PDE range, the second-order equations could be further classified

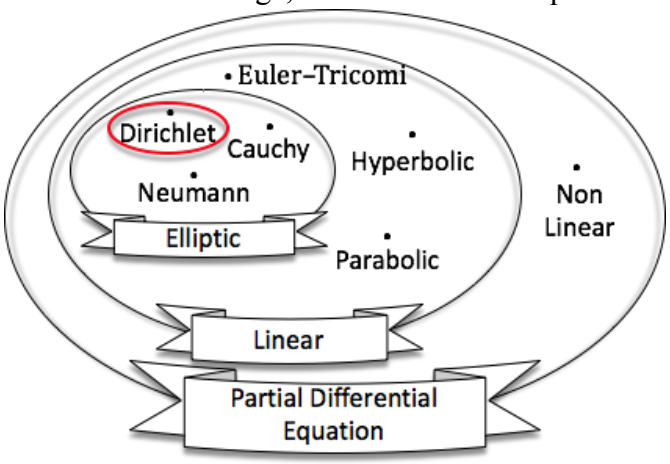

Figure S2. **Class of partial differential equations for which the Silicon Photonic Approximate Computing Engine propose an accurate solution**. We demonstrated that the engine provides an accurate solution for a steady state, second order, (Laplace-Elliptic) equation with Dirichlet (value) boundary conditions. We envision that using opportune electro-optic modulation the engine can provide accurate solutions also for problems having Cauchy and Neumann boundary conditions. Time variant equations can be solved through time discretization and successive iterations.

into 3 sub-categories determined by quadratic equation discriminant (Table 1). Here we write the homogeneous version of second-order linear PDE withc constnt coefficients as the following.

$$\mathrm{A}\frac{\partial^2 P}{\partial x^2} - B\frac{\partial^2 P}{\partial x \partial y} + C\frac{\partial^2 P}{\partial y^2} = 0 \quad (6)$$

Considering solving the second-order PDE as finding a path across the solution domain (*x,y*) and the discriminant value B^2-$4AC$ will determine whether there is a valid path passing through a general point *P* along with the second derivatives of *f(x,y)*. With a positive discriminant value, real and distinct characteristic curves can be found and make this type of PDE lies in the Hyperbolic category. If the discriminant value equals to 0, the characteristic curves are still real but repeated and this PDE is called Parabolic PDE. However, when the discriminant value is negative, the characteristic curves become complex and this type of PDE belongs to the Elliptic category which our proposed SPACE is able to solve (**Fig. S2**). All three types of PDEs have numerous applications. For example, a Hyperbolic Wave Equation could describe the electromagnetic wave propagation, while a Parabolic Diffusion Equation is often used to describe the behavior of the collective motion of small particles. And as the most well-known Elliptic Equation, the Laplace's equation could be used in electrostatics, fluid flow as well as thermal transmission. Moreover, some of the linear PDEs may contain multiple characteristics of the aforementioned classifications. For example, a Euler-Tricomi equation which is commonly used in transonic flow simulations, is elliptic when $x > 0$, parabolic when $x = 0$ and hyperbolic when $x < 0$ (Eqn. 7).

$$\frac{\partial^2 P}{\partial x^2} + x\frac{\partial^2 P}{\partial y^2} = 0 \quad (7)$$

Table S1 Classification of the second-order linear Partial Differential Equations.

Classification	Discriminant	Characteristic Curves
Hyperbolic PDE	$B^2 - 4AC > 0$	Real and distinct
Parabolic PDE	$B^2 - 4AC = 0$	Real and repeated
Elliptic PDE	$B^2 - 4AC < 0$	Complex

Last but not least, in a second-order linear Elliptic range, the PDEs could be further divided into three subclasses based on the boundary conditions (**Fig. S2**). For the Dirichlet boundary condition, the value of the solution along the domain boundary needs to be specified. For example, a fixed temperature heat source and heat sink of a heat transfer problem in a finite domain fall into this category. Differently, the Neumann boundary condition specifies the value of the derivative of a solution instead. This implies that the boundary surface needs to be smooth in order to allow the normal derivative to exist. The third boundary condition termed Cauchy boundary condition contains both Dirichlet and Neumann boundary conditions with certain weights and this could be regarded as the mix of the previous two boundary conditions.

Our demonstrated SPACE is proposed to solve the second-order linear Elliptic PDE with Dirichlet boundary condition, namely with boundary condition values all fixed (a fixed power CW laser as a constant heat source and a couple of grating couplers scatter the light to the free space with minimum reflection as a constant temperature heat sink). Nonetheless, as we mentioned in the main manuscript, SPACE also has the potential of solving other types of PDEs like the second-order Elliptic PDEs with Neumann and Cauchy boundary conditions if integrating with devices like electro-optic modulator or photodetector or both. For example, using a modulator and a photodetector in a row and feeding the photocurrent back to the modulator at the boundary, is able to reduce the light exceeding the boundary when incoming light increases and vice versa. This could give a fix derivative value which can be designed by choosing the photodiode's quantum efficiency and modulator's modulation depth.

3. 5×5 Finite Difference Method Simulation Models and Measurement Data

In this section, a step-by-step simulation process will be discussed as well as all the modeling used for describing SPACE, built in both COMSOL and Lumerical software.

The most important thing in our performance comparison is to track the accuracy from the ideal physical model simulation to the actual fabricated device measurement. Therefore, we also simulated three more models with the purpose of showing how the accuracy changes from the ideal case. All five models will be introduced one by one in the following.

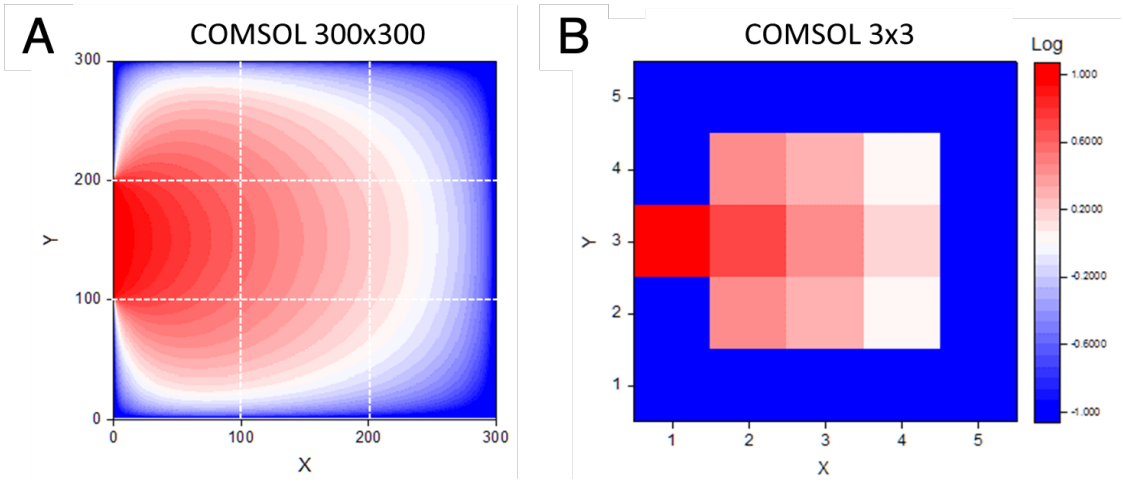

Figure S3. **Finite difference method applied to a boundary value problem**. COMSOL heat transfer simulation with a) 300×300 fine mesh and b) 3×3 coarse mesh resolution. All simulated data are normalized to unity in log-scale and the heat sink boundary is set to -1 for better color separation.

Starting from the physical model simulation. Here we first use COMSOL software to simulate the heat transfer in a 2D metal sheet which is meshed evenly into 300 by 300 nodes and compared to the 9 computing nodes at the center of our 5×5 SPACE circuit (**Fig. S3a**). Here, the additional node ad the side of the domain are used for reading the optical power at the boundary. Similarly, we choose the central 1/3 segment of the left boundary as the heat source and applied a fixed temperature (at 1 °C) boundary to it in the simulation. And for the rest of the boundary, another fixed temperature (at 0 °C) boundary is applied. In this way, we are able to simulate the actual thermal transfer profile across the sheet under the Dirichlet boundary condition. It is worth to mention that we use user-controlled mesh settings with maximum element growth rate and curvature factor all set to 1 and the size of the element set to be 1/300 of the length of the side. And to map the mesh resolution of the proposed SPACE, this 300×300 mesh result is downscaled to 3×3 as the fundamental physical baseline in our comparison (**Fig. S3b**). Here all the data are normalized to unity in log-scale in the range of [0, 1] and we use -1 to represent the boundary condition for better color separation. We understand that there is still a certain level of difference between the actual physical result and the computer software simulated data, but the difference is minimum and can be ignored.

Next, we want to see how the accuracy changes in the optical domain. To begin with, we use Lumerical Interconnect software to perform a photonic circuit simulation. In this software, we are able to build an optical black box and assign any arbitrary S-parameter to it. With this function, a perfect 1-to-3 optical splitter can be achieved with 33%: 33%: 33% splitting ratio without any back reflections, which can be considered as the ideal case of our splitter design (**Fig. S4a**). For light

propagation, a standard waveguide that supports TM mode propagation is used with its effective index (1.78921) and group index (3.578) simulated in the Lumerical Mode software. And for the date readout, Y-junction 50/50 couplers and optical oscilloscopes are used, to capture the final light intensity when the light signal reaches its steady state. This model could be considered as the theoretical upper bound of the Optical FDM and the error is caused by the non-lumped element effect of the Optical components.

To take one step further, we plug in the scattering matrix computed in 3Dimensional full-wave FDTD simulations of the KPN into the previous Lumerical Interconnect model obtaining the results illustrated in **Fig. S4 B**. The light intensity at the second and the third KPN (column) is relatively lower compared to our COMSOL baseline, which can be explained by the extra design loss of the 1-to-3 KPN. This model indicates the ideal accuracy that our proposed design could achieve.

The next model is a combination of measurement and simulation data. We first measured a single 1-to-3 splitter we fabricated at all four directions and import the S-parameter into the same Lumerical Interconnect model to simulate the whole 5x5 circuit (**Fig. S4 C**). Based on the result, light is slightly leaning towards the bottom right corner which implies that the actual splitter we fabricated is not 100% symmetric and could potentially cause a major error if same fabrication trend accumulates in the final circuit.

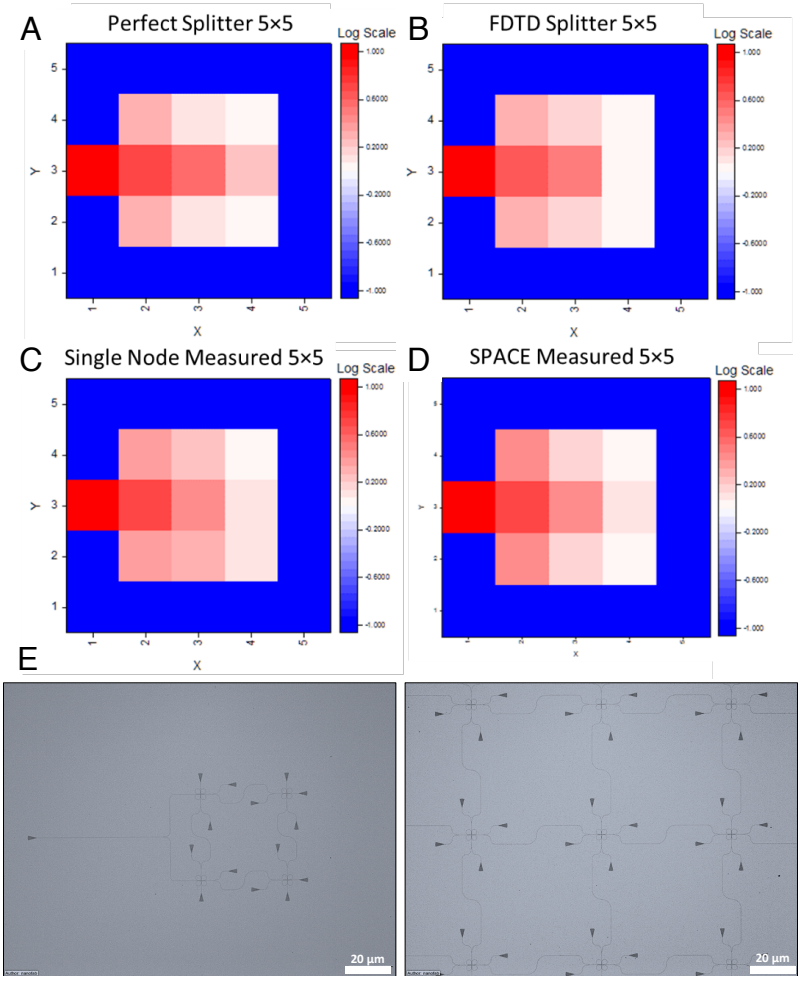

Figure S4. **Simulation and measured data of the optical 5x5 FDM using Silicon Photonic Circuits. A** Perfect splitter model, **B** FDTD splitter model, and **C** single node measured model are all simulation results from Lumerical

Interconnect. **D** The SPACE measured data is collected from the camera readout after image processing. Again, all data are normalized to unity in log-scale and the heat sink boundary is set to -1 for better color separation. **E** Optical Image of SPACE for a 2x2 (A) and 3x3 (B) FDM mesh. Each node has 4 taps in al the cardinal directions for assessing the discrete solution at each node.

At last, we plot the SPACE measurement data we collected from the Inferred images. Interestingly, there is no significant deviation to the bottom right. Since the size of the demonstrated circuit is still relatively small, any small changes in the splitting ratios at the node or the Y-junction could influence the final result. Nonetheless, it is also reasonable to conclude that SPACE model is able to provide a high degree of accuracy that closely matches the theoretical Optical FDM model.

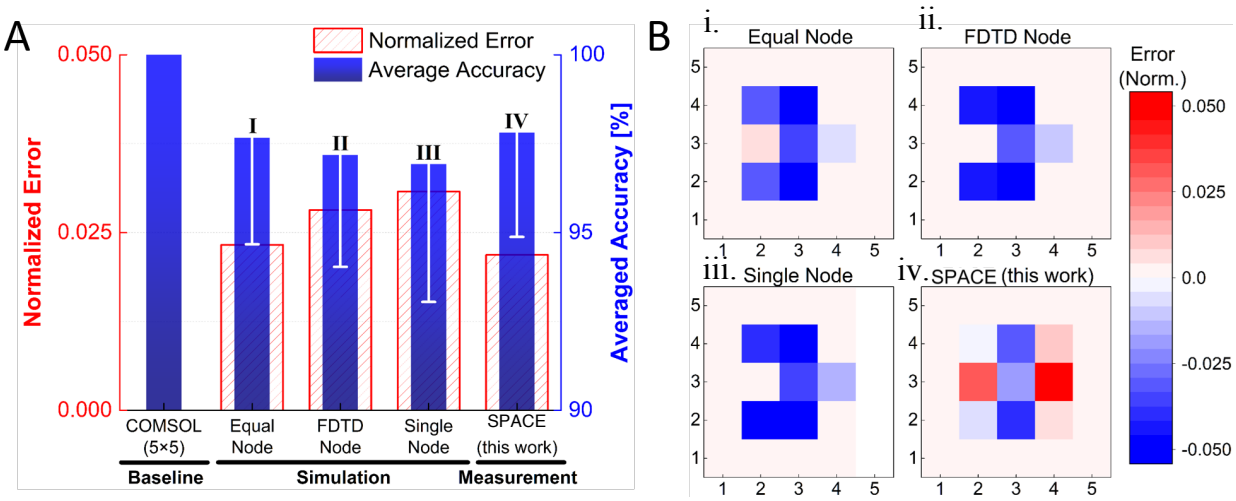

Figure S5. Accuracy performance of experimental implementation of SPACE when solving Laplace equation mapping a 5×5 FDM compared to different modeling depth. (**A**) The averaged error and accuracy comparison among COMSOL simulated electrical model (COMSOL 5×5), perfect splitting optical model (equal node), FDTD design simulation model (FDTD node), measured single component model (single node), and the 5×5 SPACE measurement model (SPACE). The negative error bars represent the accuracy level from the least accuracy node from the 5×5 FDM model. The electrical model is regarded as the baseline and scaled to 100% accuracy. From the left to right shows the step-by-step approach to the most physical model while the accuracy drops from 98.5% to 97.5%. (**B**) Normalized error heatmap between the baseline model and other models in the scale of (-0.05, 0.05). In all PIC simulations, the input light source has been set to 1 mW with optical power meter sensitivity set to -100 dBm and simulation time long enough to converge all the signal propagation delays in the network.

To summarize, the model simulated by COMSOL serves as a problem accuracy baseline case, and naturally is proportional to the mesh resolution (e.g. a 5×5 mesh COMSOL simulation has 99.95% accuracy comparing to a 300×300 mesh averaged down to a 5×5 with same initial setup, **Fig. S3**), a 5×5 discretized model is selected to make a fair comparison with other optical 5×5 models simulated and measured cases (**Fig. S5 A**). The error at each of the 9-computing nodes has been plotted in **Fig. S5 B** with the minimum node accuracy noted by negative error bars (**Fig. S5 A**). Moving towards a more experimentally meaningful simulation, the accuracy of the 5×5 FDM model can still be maintained at very high level (i.e. above 97.5%) for approximate calculations.

In both equal splitting node and FDTD node error profiles, symmetric error distribution is observed due to the balanced splitting nature of the nodes and follows with a column-by-column pattern (**Fig. S5 B-i and S5 B-ii**). In other words, consider each column as a whole block with sufficient number of nodes, then the incoming light from the previous block is basically a truncated Taylor

series of the input factored by the splitting ratio (assume a uniform equal splitting ratio) and the input to the next block is also the same Taylor series but starting from its second order. Thus, a higher splitting ratio will lead to passing more light to the next block with greater errors, which explains the accuracy of the second column's slight drop when the splitting ratio reduces from 33% (equal node model) to 23% (FDTD node model).
The highest error (~5%) is for the nodes closer to the boundary conditions (source and heat sink). This is due to the approximation performed for mimicking the trend induced by the boundary conditions which provides less accurate solutions in correspondence of the nodes close to the boundary. (**Fig. S5 B-iii and B-iv**).

4. SPACE Runtime Analysis

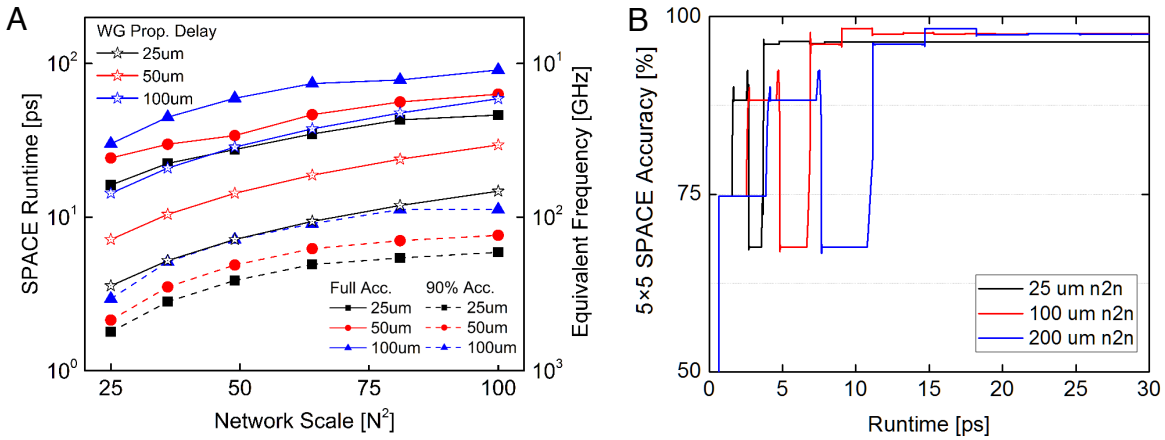

Figure S6. Runtime, bandwidth and real-time accuracy performance for SPACE engine solving a Laplace equation. A The runtime estimation considering 25 µm to 100 µm waveguide propagation delay baselines (star icons). The light propagation delay gradually dominates the total SPACE runtime for both full accuracy and 90% accuracy cases. **B** The accuracy iterates up and down represents the light propagation within the network, and eventually reaches the maximum accuracy when the light splitting signals become eligible.

The operating speed, as the other critical performance criteria of the SPACE, has also been studied in the main paper in terms of the runtime differences among different network scale and node-to-node distance. Here we replot that figure and add three more baselines of light propagation time for the same waveguide lengths (**Fig. S6 A**). The light propagation time across the network (i.e. waveguide delay) is calculated simply based on the group index of the Silicon waveguide we used with the same dimension. Comparing to the full accuracy curves (i.e. 25 µm, 50 µm, and 100 µm node-to-node distance), the gaps between the SPACE runtime and the waveguide propagation delay decrease as the network scale goes up. In other words, the light propagation time will be more dominant for larger SPACE networks runtime. It is also worth to mention that the runtime of 90% accuracy for all cases is even shorter than the waveguide propagation delay, which means the accuracy could already be achieved to a high level before the light reaches all node. This could be explained by the nature of the problem we are trying to solve. For this heat transfer on a metal sheet problem, the signal decays exponentially as propagates further. Therefore, nodes further from the input node intrinsically has orders of magnitude lower readouts and contribute less to the overall accuracy. To further study the SPACE accuracy changes over time, we use optical oscilloscopes in the Lumerical Interconnect software to record the light signal changes at all nodes. Here the overall accuracy against simulation time is plotted for a 5×5 SPACE network with again

25 μm, 50 μm, and 100 μm node-to-node distance (**Fig. S6 B**). During the simulation, the light propagates back and forth within the network and causes accuracy fluctuation. The first several big accuracy changes, in the beginning, are mainly because there are still nodes that haven't received any light signals. Then, as the light spread out evenly across the network, these iterations become more and more neglectable and result in a much smoother accuracy track. Also, we could see how each column of nodes contributes to the overall accuracy (Column 1 > Column 2 > Column 3) as we discussed before.

5. Boundary Weighted SPACE Analysis

The lumped and the non-lumped element-based circuit is one of the major differences between electrical FDM solver and optical FDM solver, as we discussed in the main paper. And the drawback to the optical FDM solver (i.e. SPACE) is that all the splitting ratios are fixed and cannot correspond to the boundary condition changes.

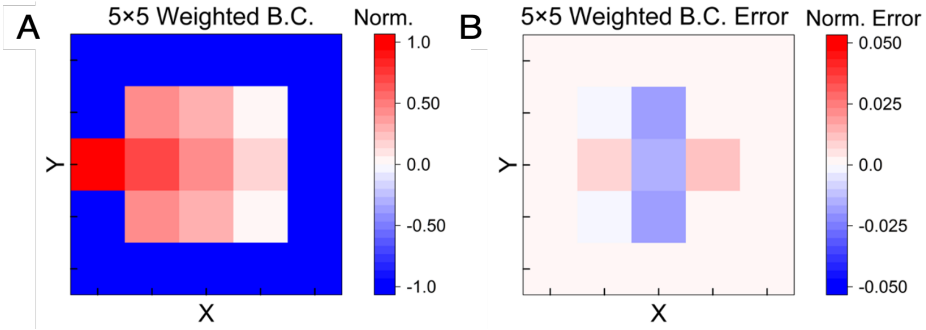

Figure S7. Weighted nodes approach for improving accuracy when solving Laplace differential equation using FDM applied to SPACE. With weighted nodes set next to the boundary condition, a 5x5 SPACE is able to provide over 99% of accuracy comparing with the same COMSOL model we simulated in the main paper. According to the error distribution heatmap, the node accuracy at four corners are further improved to make the overall accuracy 2% closer to the baseline.

Our solutions to that are to add actively tunable devices (e.g. electro-optic modulators) between each two nodes or adding tuning materials on top of the directional coupler part of each 1-to-3 splitters. Both solutions are able to change the light intensity ratios that coming out of the splitter and thus to mimic the lumped element effect of electronic devices. Here we test the case that only changes the splitting ratios of the nodes that are connecting to the boundary condition. To be more specific, the splitting ratio of the nodes on the edges is changed from 33%: 33%: 33% to 10%: 10%: 80% where 80% of light be absorbed by the boundary; while the splitting ratio of the corner nodes is changed to 20%: 40%: 40% with both 40% of light goes into the boundary. In this way, we are able to determine whether forcing the splitting ratios at each node to emulate the lumped element circuit could help to improve the result. By changing the splitting, more light will be routed to the boundary and absorbed, which simulates a scenario that closer to the actual problem. As a result, the accuracy is improved to 99.2% which is very close to the COMSOL baseline that we set (**Fig. S7**). The rest 0.8% accuracy could be further improved by more precisely control the splitting ratios adjacent to the boundary condition as well as the center node. In addition, this once again proves that adding additional active tuning mechanisms at each node that enables the full reconfigurability is a possible way to mimic the lumped element-based circuit.

The other variable that can be weighted is the coupling ratio of the node. Here, we simulated three difference cases which use 33%:33%:33%, 50%:0%:50%, and 0%:100%:0% splitting ratios

respectively. As the splitting ratio gradually deviates from equal splitting, the final accuracy drops from over 97% down to 68% (**Fig. S8**). Based on this result, we verify that equal splitting ratio is able to provide the highest initial accuracy.

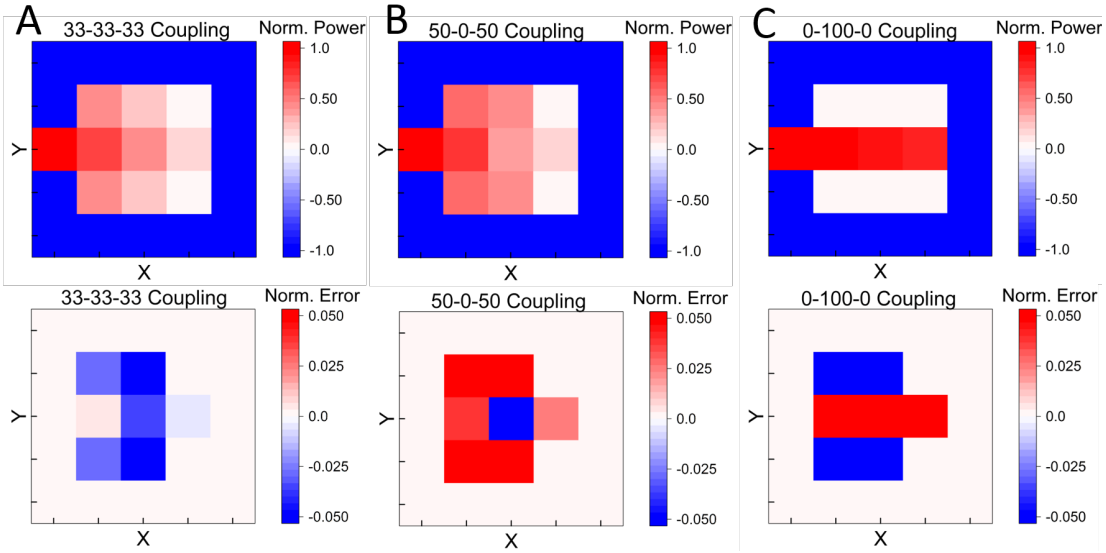

Figure S8. **Accuracy analysis for different splitting ratios.** The cases considered are (A) 33%:33%:33%, (B) 50%:0%:50% and (C) 0%:100%:0% node coupling ratios. The overall accuracy of these three models are 97.7%, 92.5% and 68.3% respectively, and this shows that using equal splitting ratio can be regarded as the best initial setting for SPACE for the best performance.

We extended our study to a a boundary value problem in which higher temperature is applied at the top left corner of the FDM mesh, and all the other borders are set to a lower temperature. (**Fig. S9**)

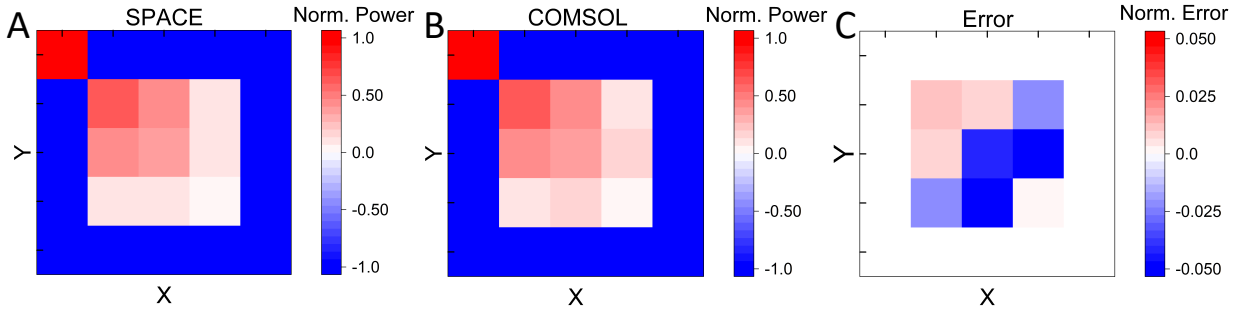

Figure S9. **Simulation of an optical 5x5 FDM of a boundary value problem using Silicon Photonic Circuits.** Simulation results of a Laplace PDE from (A) the photonic engine SPACE (Lumerical Interconnect) and (B) COMSOL. The boundary conditions of the PDE are Dirichlet's in which high temperature (T=100ºC) is assigned to the top left node of the mesh and T=0 to all the other boundaries. All data are normalized to unity in log-scale and the heat sink boundary is set to -1 for better color separation. (C) Error computed by the photonic engine when solving the PDE compared to a discrete solution which exploits the same mesh density. Error is within ±5%.

6. SPACE configuration library for solving heat transfer for different materials

In this section we ought to solve a Laplace homogeneous partial differential equation applied to domains with different thermal properties using SPACE. We then compare the solutions obtained using numerical iterative method and SPACE. For this purpose, two software are chosen:

COMSOL Multiphysics and Lumerical Interconnect, used for simulating heat transfer and light propagation at the interconnect level, respectively.

In order to obtain a library of configuration for our SPACE engine, we try to map the heat propagation in three films made by three different materials: Aluminum, Vanadium and Calcarb CVD 20 (an insulator material consisting of carbon fiber).

The domain consists of a square geometry. A higher temperature is applied at the boundary of a small subdomain placed in the top corner of the geometry, set to be a (373 K) heat source, simultaneously all the remaining boundaries are set to be 0°C, which represent the heat sink in this model. As previously discussed, we use COMSOL Multiphysics for benchmarking the accuracy of the discretized solution obtained by SPACE. The geometry is meshed according to a triangular mesh type. In order to resolve the temperature distribution on the proposed, the mesh size must be smaller than the minimum element of the model, which for this case is the heat source square. However, the simulation time decreases, likely, polynomial for reducing the mesh size. For a square mesh, with side length N and a number of M iterations, for instance, the run-time for convergence would scale as $2NM$. To test this, 25 uniformly distributed (equally spaced) points in the geometry are sampled for extrapolating discrete value to compare to the discrete solutions proposed by SPACE at lower mesh density.

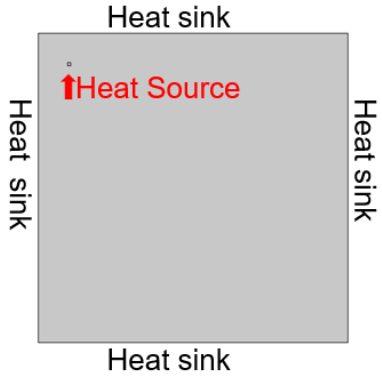

Figure S10-a. The geometric setting of thermal transfer simulation, a 5 by 5 square with one heat source at the top left corner and heat sinks at boundaries.

Second, the computing engine of thermal simulation is described by following equation:

$$d_z \rho C_p \mathbf{u} \cdot \nabla T + \nabla \cdot \mathbf{q} = d_z Q + q_0 + d_z Q_{ted} \quad (1)$$

$$\mathbf{q} = -d_z k \nabla T \quad (2)$$

Where ρ represents the density of material(kg/m^3), Q is the heat source, u is the velocity, q is the heat flux and k is the thermal conductivity (W/(m·k)). In our stationary case, dz is out-of-plane thickness, C_p represents the specific heat capacity(J/(kg·k)), and Q_{ted} is the thermoelastic damping.

It is worth mentioning that the properties are both material dependent and temperature dependent.

A representative temperature distribution map for the thermal distribution on an aluminum film is presented (**Fig. S10-b**). We sample the values of the temperature on 25 points. Thus, these values form a data set representing the heat transfer map of each material.

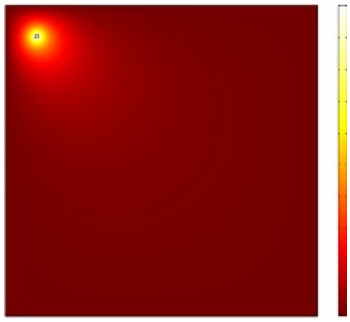

Figure S10-b. The heat map of Aluminum, ranging from 0K to 373.15 K.

Furthermore, an optical transfer simulation is needed for comparing with heat transfer simulation. In Lumerical Interconnect software, a 5x5 optical mesh was built to imitate the mesh structure of heat transfer. At crossing nodes, we select scattering matrix parameter (S-parameter) to perform the optical characteristic of equal splitter. Considering every node has four directions, regardless which direction the light propagates through, the light will split into other three directions with equivalent value. In between two nodes, the extinction ratio of modulators can be used for altering the solutions and reprogramming the engine. In the model, a 30mW laser light source is placed at the left top corner, exactly like the heat source in thermal simulation.

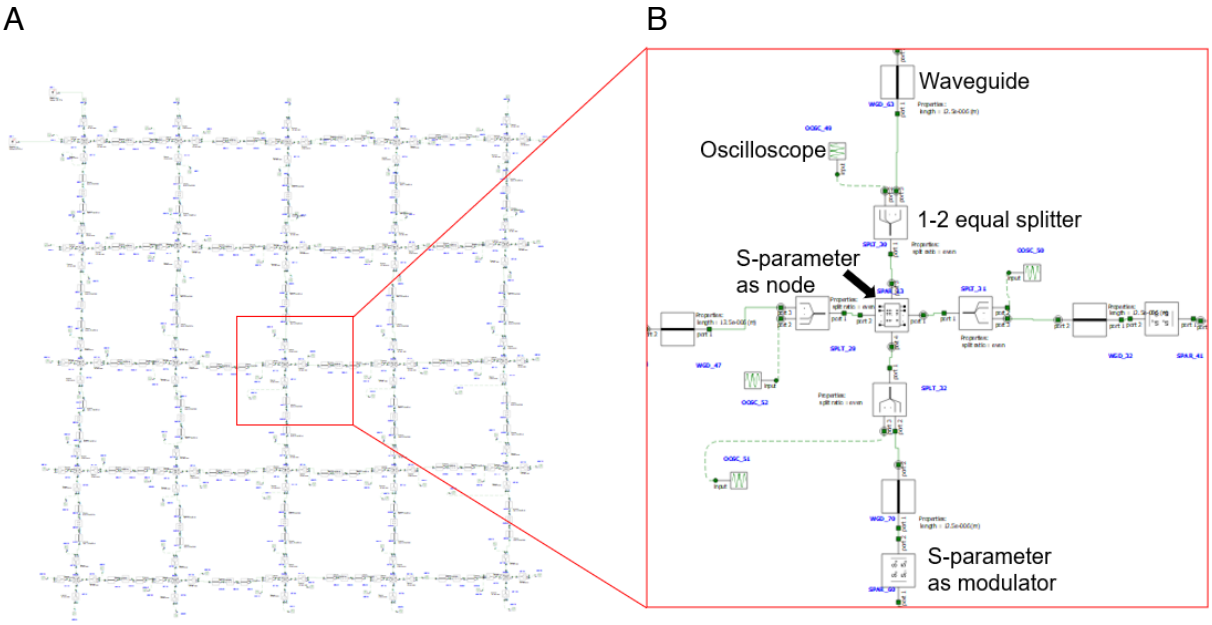

Figure S10-c. (A) A general structure of the interconnect simulation model of SPACE, which is mapping a meshx FDM. Light propagates from a continuous wave laser source located at left top corner. (B) A detailed image of node structure. We can read and add the data of four oscilloscopes connected with an equal splitter around the node to obtain the power through this node.

After achieving the data sets from the previous modelling and emulation, considering being quantities incoherent quantities in terms of measure units (Temperature and optical power), we opted for a normalization (0-1). Notably, limited by nowadays modulator technology, the maximum extinction ratio of modulator can be set to a maximum of a 10dB. For a completely passive configuration of SPACE the average accuracy is significantly lower than 70%. Therefore,

we decided to obtain different configurations for each material, with the further constrain of providing the same level accuracy.
The configurations considered are reported in **Fig. S10-d**, in which only the modulators in between the input source and the neighboring node are activated.

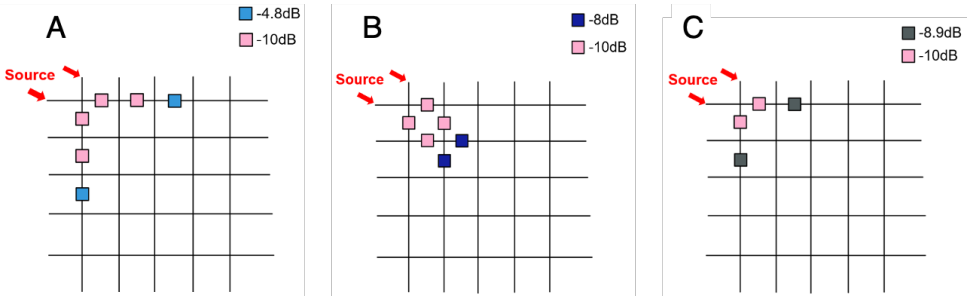

Figure S10-d. SPACE mapping temperature distribution in Aluminum (A), Vanadium (B) and Calcarb (C).

After analyzing all the possible permutations, and comparing the interconnect simulations with the numerical results, we obtain the distribution of error for each node of the mesh and the average accuracy of different materials when we use SPACE as solver. Our aim in this section is not to obtain the overall best accuracy, but concurrently maximize accuracy while obtaining unique configurations for specific materials.

Material	Model (A) Error Map	Model (B) Error Map	Model (C) Error Map
Aluminum	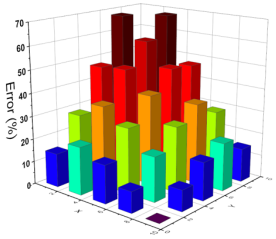 70.00%	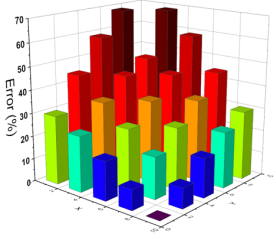 67.26%	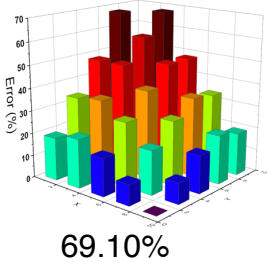 69.10%
Vanadium	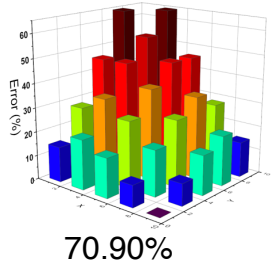 70.90%	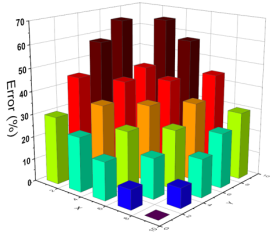 68.15%	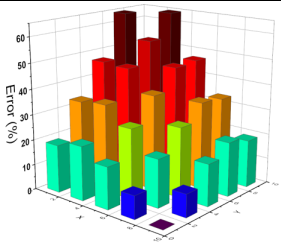 70.00%
Calcarb CVD 20	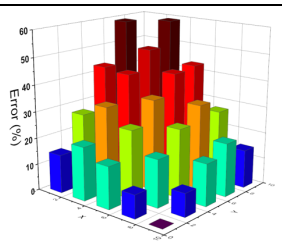 72.75%	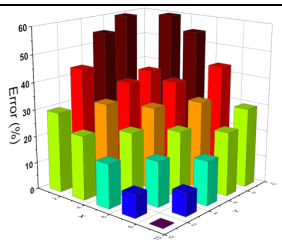 70.00%	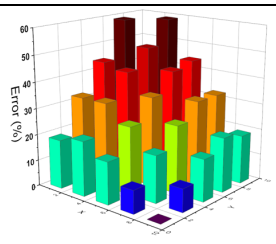 71.84%

Figure S10-e Error distribution when solving PDE in Eq 1. for the configurations illustrated in **Fig. S10d.**

It can be noticed that the most considerable inaccuracies are for the nodes in proximity of the source. This can be ascribed to the approximation used for describing the thermal gradient induced by the boundary conditions, obtained by modulating the inter-node linear correlation. In this case, unlike the simulation proposed in the main manuscript, the heat source is within the main geometry, in close proximity with a heat sink, forcing an abrupt thermal gradient. The equivalent optical power distribution provided by SPACE cannot straightforwardly mimic this trend, considering the limited dynamic range of the modulators (ER=10dB), thus resulting in a significantly less accurate solution.